

New magnetic data indicate successive ridge jumps and rotations of seafloor spreading in the South China Sea

Jiabiao Li¹, Qingsheng Guan², Tao Zhang³, Brian Taylor⁴, and Jinyao Gao⁵

¹Second Institute of Oceanography, State Oceanic Administration

²Nanjing University

³Second Institute of Oceanography, Ministry of Natural Resources, China

⁴University of Hawaii at Manoa

⁵State Oceanic Administration

November 22, 2022

Abstract

New shipborne surveys provide a closely spaced magnetic anomaly dataset covering the East Subbasin (ESB) of the South China Sea (SCS). Magnetic anomalies of seafloor spreading are identified using the dataset supplemented with previous data and age constraints from recent International Ocean Discovery Program Expeditions 349 and 367/368 holes. We present a high-resolution oceanic crustal age model and associated magnetic lineations of the ESB based on identified magnetic anomaly picks. Seafloor spreading in the ESB initiated at ~ 30 Ma (C11n) and terminated at ~ 16 Ma (C5Br). The spreading direction has experienced a gradual counterclockwise rotation between C6Cr and C5Er and a significant counterclockwise rotation at C5Dr. The spreading rotations reorganized the orientation and segmentation of the spreading ridge, resulting in the formation of a series of S-shaped fracture zones. The interpretation of the magnetic lineations reveals that three southward ridge jumps occurred at C9r, C8n, and C7n and a synchronous jump occurred at C5Dr. Three southward ridge jumps contributed to a total difference of ~ 184 km in the distance between the two flanks and left the paired magnetic lineations C10r–C7r on the present-day north flank. The synchronous jump caused the spreading ridge to rotate rapidly counterclockwise and obliquely intersect the existing seafloor. We postulate that these ridge jumps and rotations are common processes during seafloor spreading reorientation and are dynamic responses to the plate or microplate tectonics around the SCS.

1 **New magnetic data indicate successive ridge jumps and rotations of**
2 **seafloor spreading in the South China Sea**

3 **Qingsheng Guan^{1,2,3}, Tao Zhang^{2,3*}, Brian Taylor⁴, Jinyao Gao^{2,3}, Jiabiao Li^{2,3*}**

4 ¹Collaborative Innovation Center of South China Sea Studies and School of
5 Geographic and Oceanographic Sciences, Nanjing University, Nanjing, China.

6 ²Second Institute of Oceanography, Ministry of Natural Resources, Hangzhou, China.

7 ³Key Laboratory of Submarine Geosciences, Ministry of Natural Resources,
8 Hangzhou, China.

9 ⁴School of Ocean and Earth Science and Technology, University of Hawaii at Manoa,
10 Honolulu, USA.

11

12 Corresponding authors: Jiabiao Li and Tao Zhang,

13 (jbli@sio.org.cn; tao_zhang@sio.org.cn)

14

15 **Key Points:**

- 16 • We present a new high-resolution oceanic crustal age model of the South
17 China Sea.
- 18 • Seafloor spreading in the South China Sea is characterized by successive
19 ridge jumps and counterclockwise rotations of seafloor spreading.
- 20 • Frequent ridge jumps and rotations of seafloor spreading may be dynamic
21 responses to the plate tectonics around the South China Sea.

22 **Abstract**

23 New shipborne surveys provide a closely spaced magnetic anomaly dataset covering
24 the East Subbasin (ESB) of the South China Sea (SCS). Magnetic anomalies of seafloor
25 spreading are identified using the dataset supplemented with previous data and age
26 constraints from recent International Ocean Discovery Program Expeditions 349 and
27 367/368 holes. We present a high-resolution oceanic crustal age model and associated
28 magnetic lineations of the ESB based on identified magnetic anomaly picks. Seafloor
29 spreading in the ESB initiated at ~30 Ma (C11n) and terminated at ~16 Ma (C5Br). The
30 spreading direction has experienced a gradual counterclockwise rotation between C6Cr
31 and C5Er and a significant counterclockwise rotation at C5Dr. The spreading rotations
32 reorganized the orientation and segmentation of the spreading ridge, resulting in the
33 formation of a series of S-shaped fracture zones. The interpretation of the magnetic
34 lineations reveals that three southward ridge jumps occurred at C9r, C8n, and C7n and
35 a synchronous jump occurred at C5Dr. Three southward ridge jumps contributed to a
36 total difference of ~184 km in the distance between the two flanks and left the paired
37 magnetic lineations C10r–C7r on the present-day north flank. The synchronous jump
38 caused the spreading ridge to rotate rapidly counterclockwise and obliquely intersect
39 the existing seafloor. We postulate that these ridge jumps and rotations are common
40 processes during seafloor spreading reorientation and are dynamic responses to the
41 plate or microplate tectonics around the SCS.

42

43 **1 Introduction**

44 The South China Sea (SCS) is the largest marginal basin in Southeast Asia and has
45 experienced an almost complete Wilson cycle since the early Cenozoic. Studies of the
46 SCS can provide important information for reconstructing the Cenozoic tectonics of
47 Southeast Asia and improve the understanding of the evolution of marginal basins.
48 Although the seafloor spreading history and geodynamics of the SCS have been
49 extensively studied, some key issues remain controversial or unclear: first, the debates
50 about the age of seafloor spreading, such as ~30–16 Ma (Briais et al., 1993; Taylor &
51 Hayes, 1983), ~32–20.5 Ma (Barckhausen et al., 2004, 2014), and ~33–15 Ma (Li et
52 al., 2014); second, the asymmetric spreading processes during the early spreading stage
53 (Briais et al., 1993; Ding et al., 2018); third, the locations and trends of the major
54 fracture zones in the SCS (Ruan et al., 2016; Sibuet et al. 2016; Yao, 1995); and finally,
55 several potential geodynamic mechanisms for the opening of the SCS, including the
56 slab pull model (Holloway, 1982; Taylor & Hayes, 1980, 1983), Indochina extrusion
57 model (Briais et al., 1993; Tapponnier et al., 1982). A robust crustal age model and
58 associated magnetic lineations could provide crucial insights into the above major
59 unsolved controversies. However, due to intense post-spreading volcanism and lack of
60 microfossil or radiometric ages, previous magnetic lineation patterns based on
61 relatively sparse magnetic data have been debated (e.g., Barckhausen et al., 2004, 2014;
62 Briais et al., 1993; Li et al., 2014; Taylor & Hayes, 1983; Zhang et al., 2012).

63 In this paper, we use recently collected sea surface magnetic data to establish a set
64 of high-resolution magnetic lineations and a new crustal age model for the East Sub-
65 basin (ESB) of the SCS. Based on the magnetic anomalies, we identify successive ridge
66 jumps and describe the detailed jumping processes of these spreading ridges. Combined
67 analyses of magnetic anomalies, vertical gravity gradient (VGG), and geomorphic
68 features, we determine the locations and trends of the major fracture zones in the SCS.
69 On the basis of the magnetic lineations, we decipher the continuous counterclockwise

70 rotations of seafloor spreading. We further discuss the implications of seafloor
71 spreading rotations for the geodynamic processes of the evolution of the SCS.

72 **2 Geological Background**

73 The SCS is situated at the junction of the Eurasian, Indo-Australia, and Philippine
74 plates (Figure 1). Its surroundings include three major types of continental margins.
75 The northern and southern parts of the SCS are passive rift continental margins. The
76 eastern part is bounded by the Manila Trench, where the SCS slab subducts 400~500
77 km beneath the Philippine plate (Wu et al, 2016). The western part is bounded by a
78 strike-slip fault zone, along which Indochina was extruded by the collision between the
79 Indian and Eurasian plates (Leloup et al., 2001; Tapponnier et al., 1982, 1990).

80 The oceanic basin of the SCS has been divided into the ESB, the Southwest
81 Subbasin (SWSB), and the Northwest Subbasin (NWSB). The ESB is separated from
82 the SWSB and the NWSB by a major Zhongnan fracture/fault zone (Sibuet et al., 2016;
83 Yao, 1995). However, the location and trend of the Zhongnan fracture/fault zone are
84 still controversial. Based on morphological and seismic data, Yao (1995) proposed that
85 the Zhongnan fault is an N–S-trending fault that extends along 116°E northward to
86 south China margin and southward to Borneo. Similarly, on the basis of swath-
87 bathymetric data, Sibuet et al. (2016) postulated that the Zhongnan fault is a generally
88 NNW–SSE-trending fracture zone, which contain a series of parallel fracture zones.
89 Ruan et al. (2016) suggested that the Zhongnan fault is an NW–SE-trending fracture
90 zone near 116°E with a width of 40–60 km based on wide-angle seismic profiles.

91 **2.1 Crustal age models of the SCS**

92 The oceanic crustal age of the SCS has been estimated by the identification of
93 magnetic anomalies and dating from the International Ocean Discovery Program
94 (IODP). Three major age models have been established based on magnetic data from
95 the SCS. Following Taylor and Hayes (1980, 1983), Briaies et al. (1993) suggested that
96 the SCS spreading occurred from ~30 Ma to ~16 Ma (revised based on the geomagnetic

97 polarity time scale (GPTS) of Gee and Kent (2007)). By reinterpreting the magnetic
98 anomalies from different magnetic data, Barckhausen et al. (2004, 2014) proposed that
99 seafloor spreading in the SCS initiated at 32 Ma and ceased at 20.5 Ma. Li et al. (2014)
100 jointly analyzed the deep-tow magnetic data and IODP Expedition 349 cores and
101 estimated that the seafloor spreading duration in the SCS was ~33–15 Ma.

102 IODP Expeditions 349 and 367/368 drilled at the northern continent-ocean
103 boundary (COB) and near the fossil ridge in 2014 and 2017, respectively (Figure 1).
104 On the northern COB, Site U1500 and Site U1502 from IODP Expeditions 367/368
105 were cored into the igneous basement rocks that were directly overlain by late
106 Oligocene (~27 Ma) and early Oligocene (~30 Ma) sediments, respectively (Larsen et
107 al., 2018; Sun et al., 2018). The core at Site U1435 from IODP Expedition 349
108 penetrated through a breakup unconformity (~33 Ma), although it did not reach the
109 igneous basement (Li et al., 2015). In the area close to the fossil ridge, Sites U1431,
110 U1433, and U1434 from IODP Expedition 349 cored into the igneous basement, and
111 $^{40}\text{Ar}/^{39}\text{Ar}$ dating of the three sites yielded ages of ~15 Ma, ~17.3 Ma, and ~16.3 Ma,
112 respectively (Koppers, 2014). However, the age of Site U1431 is slightly younger than
113 the age of the overlying sedimentary layer, which may have resulted from the basalt
114 intruding the already deposited sediments after the cessation of spreading (Sibuet et al.,
115 2016).

116 **2.2 Seafloor spreading in the SCS**

117 The opening of the SCS basin from the northeast to the southwest experienced two
118 stages. The first stage was initiated by the opening of the ESB and the NWSB, but
119 seafloor spreading of the NWSB lasted only ~2–2.6 Ma (Briais et al., 1993; Zhang et
120 al., 2012). In the ESB, possible ridge jumps are observed and cause asymmetry in the
121 geometry and magnetic anomalies (Briais et al., 1993; Ding et al., 2018). However,
122 only the ridge jump at C7/C6C has been previously identified by magnetic data
123 (Barckhausen et al., 2004, 2014; Briais et al., 1993; Li et al., 2014). This ridge jumped
124 southward by approximately 20 km (Li et al., 2014), contributing to a ~40 km difference

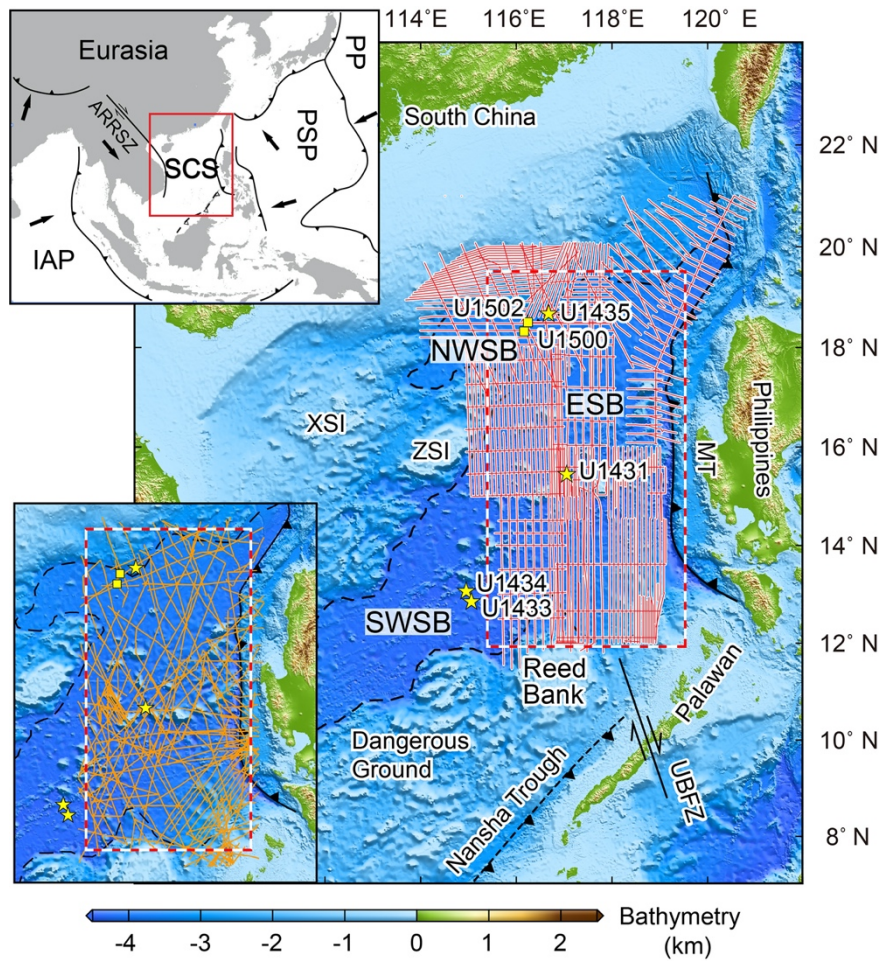
125 between the northern and southern flanks. After the ridge jump, seafloor spreading
126 propagated progressively southwestward, and the second stage began (Li et al., 2012).

127 Li et al. (2002) analyzed the trends of the fracture zones in the ESB and suggested
128 that the spreading direction of the SCS might have been N137° during the late spreading
129 stage. Recently, Sibuet et al. (2016) proposed that the SCS experienced three spreading
130 directions: N175°, N165°, and N145°, based on magnetic lineations and the seafloor
131 fabric. This view is supported by the major axis orientations of the intraplate seamounts
132 in the SCS (Fan et al., 2017).

133 **2.3 Geodynamic models of the SCS opening**

134 Two end-members driving force models have been proposed for the SCS opening,
135 involving the slab pull model (Holloway, 1982; Taylor & Hayes, 1980, 1983) and
136 Indochina extrusion model (Briais et al., 1993; Tapponnier et al., 1982, 1990). In slab
137 pull model, the southward subduction of the Proto-SCS (PSCS) drove the rifting and
138 opening of the SCS. Following the detachment of the Dangerous Grounds and North
139 Palawan blocks from the South China block, seafloor spreading in the SCS initiated
140 (Zahirovic et al., 2014). Seafloor spreading in the SCS ceased when these blocks
141 collided with Borneo (Taylor & Hayes, 1980, 1983).

142 Alternatively, the Indochina extrusion model hypothesizes that several hundred
143 kilometers of southeastward extrusion of Indochina along the Ailaoshan-Red River
144 shear zone (ARRSZ) triggered the opening of the SCS in a pull-apart manner (Briais et
145 al., 1993; Tapponnier et al., 1982; 1990). The large-scale left-lateral strike-slip
146 movements along the ARRSZ were limited to ~35–17 Ma based on the cooling ages of
147 metamorphic rocks from the ARRSZ (Gilley et al., 2003; Leploup et al., 2001; Schärer
148 et al., 1990). The offshore prolongation of the ARRSZ extends southward along the
149 Vietnamese margin, and was named as East Vietnam Boundary Fault Zone (EVBFZ)
150 (Fyhn et al., 2009a, 2009b). The left-lateral movements along the EVBFZ ceased
151 around the middle Oligocene due to a temporary change from transtension to
152 transpression (Fyhn et al., 2009b).



154

155 **Figure 1.** Location of the SCS and tracks of magnetic profiles. Red box marks the
 156 research area of this study. Red lines indicate sea surface magnetic tracks. Yellow stars
 157 indicate the drilling sites of IODP Expedition 349 (Li et al., 2015). Yellow squares
 158 indicate the drilling sites of IODP Expeditions 367 and 368 (Sun et al., 2018). Black
 159 dashed lines indicate the continent-ocean boundary determined from the vertical
 160 gravity gradient (Sandwell et al., 2014). The upper left inset shows the plate tectonic
 161 setting. The lower left inset shows supplementary magnetic tracks obtained from the
 162 National Centers for Environmental Information. XSI, Xisha Islands; ZSI, Zhongsha
 163 Islands; ARR SZ, Ailaoshan-Red River Shear Zone; MT, Manila Trench; UBFZ,
 164 Ulugan Bay Fault Zone; IAP, Indo-Australian Plate; PSP, Philippine Sea Plate; PP,
 165 Pacific Plate.

166 The high-resolution sea surface magnetic data for the ESB, composed of 389
167 magnetic profiles with a total length of 57,600 km, were collected between 1999 and
168 2014 (Figure 1). The magnetic data have denser sampling, better navigation, and greater
169 geographic coverage than previous data. The trend of most track lines is N–S, which is
170 consistent with the spreading direction of the SCS. The mean spacing of the track lines
171 is approximately 10 km. A cesium and/or proton precession magnetometer was towed
172 behind a research vessel at a distance of 2.5–3 times the length of the vessel during the
173 investigations. The magnetic data are processed with the following three steps (Gao &
174 Liu, 2014). First, the magnetic data are corrected for diurnal variations with the data
175 from nearby temporary magnetic observatories. Second, the magnetic anomaly is
176 calculated by removing the international geomagnetic reference fields (IGRF)
177 (Thébault et al., 2015). Finally, the magnetic anomaly of each profile is shifted by a
178 constant value to minimize the crossover errors according to the least-squares criterion.
179 The root-mean-square error of the processed magnetic data at crossover points is 12.9
180 nT.

181 The collected sea surface magnetic data are combined with supplementary data
182 from the National Centers for Environmental Information to constitute the final
183 magnetic dataset (Figure 1). After applying a constant shift to each profile, the root-
184 mean-square error of the magnetic dataset at crossover points is 19 nT. A magnetic
185 anomaly map of the ESB is produced by gridding the magnetic dataset using the
186 Generic Mapping Tools software (Wessel et al., 2019) (Figure 3). Meanwhile, we also
187 determine the COB of the SCS based on the version 28 of VGG from Sandwell et al.
188 (2014).

189 We select the nearly N–S-trending profiles from the magnetic dataset to identify
190 magnetic anomalies. Magnetic anomalies are identified through the stacking of
191 magnetic profiles, identification of the stacked profiles, and identification of each
192 profile. The magnetic anomalies on each profile with relatively large amplitudes and
193 similar shapes are assumed to be caused by the same geomagnetic reversals. The

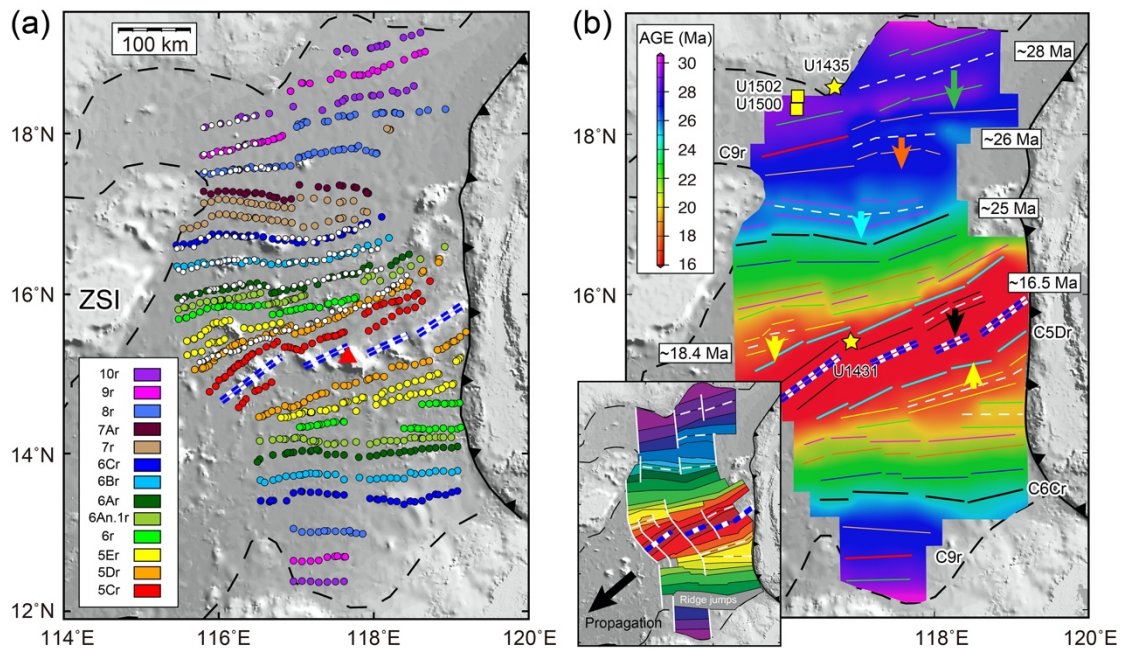
194 magnetic profiles are stacked based on the selected magnetic anomalies associated with
195 the same geomagnetic reversals (Figures S2 and S3). Along the stacked profile, the
196 signals of the Earth's magnetic field reversals are enhanced, and signals generated by
197 local tectonic and magmatic activities are suppressed (Zhang et al., 2019).

198 We perform forward modeling using the software MODMAG (Mendel et al., 2005)
199 under the constraints of dating from the IODP Expeditions 349, 367, and 368 sites
200 (Koppers, 2014; Li et al., 2015; Sun et al., 2018). The GPTS model of Gee and Kent
201 (2007) is used in the forward modeling. The magnetization of the magnetic sources is
202 assumed to be 5 A/m. The thickness of the magnetic layer is assumed to be 0.7 km to
203 match the amplitudes of the magnetic anomalies. The contamination coefficient R is
204 set to be 0.7 ($0 < R < 1$, with 1 for no contamination) to better match the shapes of the
205 magnetic anomalies. The mean ambient declination and inclination of the fossil ridges
206 at 117°E are -1.5° and 17.5° , respectively.

207 The shapes and amplitudes of the magnetic anomalies along the synthetic profile
208 are visually compared to those of the stacked profile to determine the best-fit
209 geomagnetic polarity reversal sequences. The coherent magnetic anomaly picks of each
210 profile are then identified based on the sequences of the stacked profile.

211 **4 Results**

212 **4.1 Crustal age model**



213
214 **Figure 2.** Magnetic anomaly picks and oceanic crustal ages in the ESB. (a) Solid circles
215 indicate the magnetic anomaly picks identified from the magnetic profiles. Open circles
216 indicate the magnetic anomaly picks on the south flank rotated onto the north flank.
217 Blue double dashed lines indicate possible locations of the fossil ridges. The
218 background is shaded topography (Tozer et al., 2019). Red triangle is where the
219 spreading directions and rates of the ESB are computed in section 4.4. (b) Oceanic
220 crustal ages of the ESB inferred from magnetic lineations. White dashed lines mark the
221 locations of the ridge jumps. The inset indicates the postulated tectonic evolution of the
222 ESB. White lines in the inset indicate potential fracture zones.

223 We identify 13 reverse polarity chrons (C10r–C5Cr) along magnetic anomaly
224 profiles in the ESB (Figure 2a). The oldest magnetic anomaly close to the northern
225 COB is C11n (Figure S2a), as originally identified by Taylor and Hayes (1980, 1983),
226 indicating that seafloor spreading in the ESB initiated at C11n (~30 Ma). The magnetic
227 lineation pattern consists of 856 magnetic anomaly picks, which is several times the
228 numbers in previously studies (Barckhausen et al., 2004, 2014; Briais et al., 1993; Li et

229 al., 2014; Taylor et al., 1983). More picks and smaller mean spacing between picks
230 along the isochrones improve the resolution of the magnetic lineation pattern.

231 Each magnetic lineation is assigned an age based on the middle of the associated
232 polarity epoch of the GPTS. The magnetic lineations are then associated with crustal
233 ages between ~30 Ma and 17 Ma. The distance between the youngest magnetic
234 lineations C5Cr (17 Ma) and the fossil ridge is ~22 km. Given a half spreading rate of
235 22.8 mm/yr (between C6Ar and C5Dr) (Figure 5b), seafloor spreading ceased at ~16
236 Ma. An oceanic crustal age grid (0.5'×0.5') of the ESB is then created using the
237 minimum curvature method (Figure 2b).

238 **4.2 Identification of ridge jumps**

239 The two flanks of the fossil ridge in the ESB exhibit two conspicuous negative
240 magnetic anomalies (M1 and M2 in Figure 3) which are conjugated to each other (Briais
241 et al., 1993; Li et al., 2014; Taylor & Hayes, 1980, 1983). According to the numbers
242 and distribution of magnetic lineations, the oceanic domain between M1/M2 and the
243 COBs on both flanks can be divided into the eastern and western parts along the
244 magnetic lineation offset near 117°E in the north flank and the magnetic lineation offset
245 near 118°E in the south flank (Figures 3a and 3b).

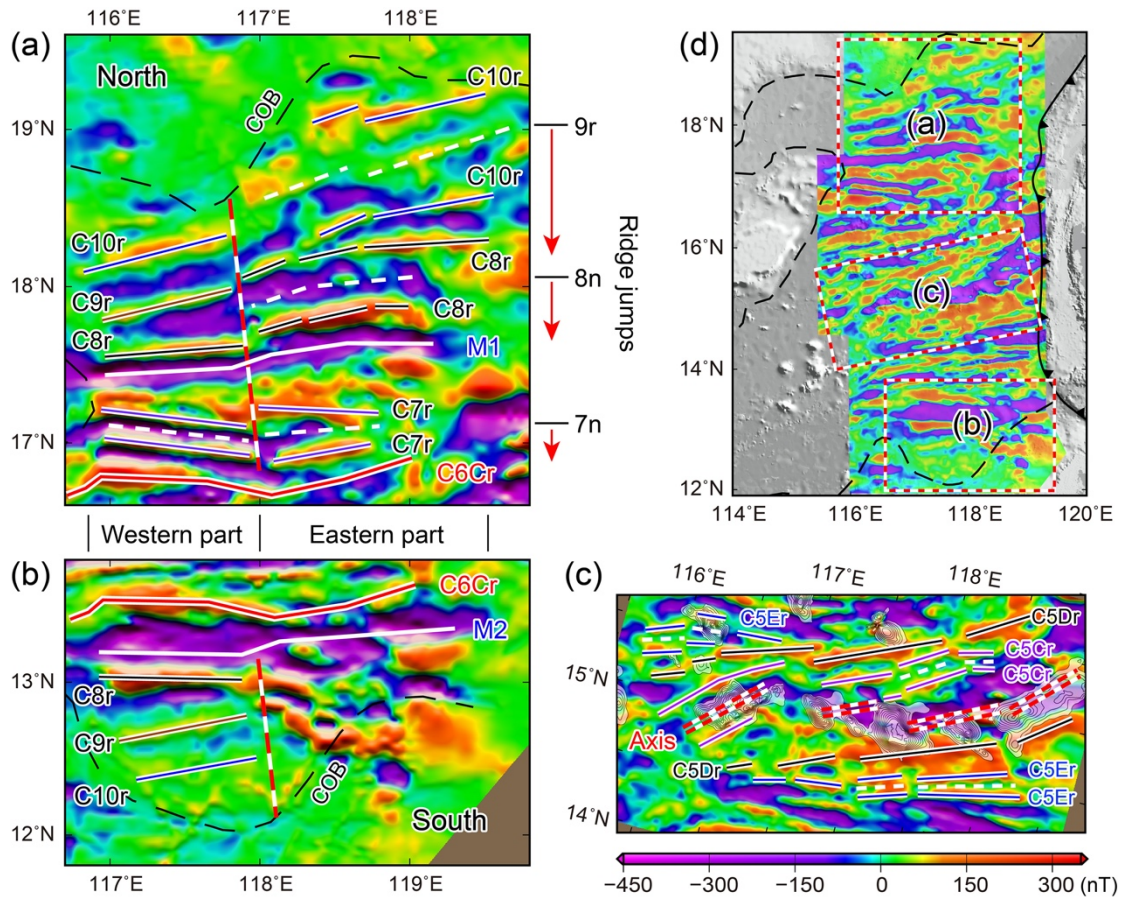
246 Each western part of the two flanks contains three positive magnetic anomalies,
247 although the magnetic lineation close to the COB on the south flank is blurred. The
248 profiles crossing these magnetic anomalies show a conjugate anomaly pattern. The
249 distances between M1/M2 and the COBs on both flanks are also roughly equal. These
250 observations indicate that the sequence of magnetic anomalies in the western parts is
251 generated by normal oceanic crust accretion. We interpret the first three positive
252 magnetic anomalies as C10r, C9r, and C8r under the constraints of age from hole U1502
253 (Sun et al., 2018). In addition, there are two anomalous magnetic anomalies between
254 anomalies C8 and C6Cr on the north flank, but they are missing in the conjugate area
255 on the south flank (Figures 3a and 3b). We infer that a southward ridge jump may have
256 occurred between anomalies C8r and C6Cr. Based on forward modeling, we interpret

257 two anomalous magnetic anomalies as paired C7r caused by the ridge jump at C7n (~25
258 Ma).

259 In the eastern part, the north flank between M1 and the northern COB has a width
260 of ~190 km and contains five positive magnetic lineations (Figure 3a). The south flank
261 between M2 and the southern COB has a width of ~45 km, and there are no prominent
262 and continuous magnetic lineations (Figure 3b). These differences between the two
263 flanks indicate asymmetric seafloor spreading during the early spreading stage. The
264 asymmetric spreading rates cannot explain the absence of magnetic lineations between
265 M2 and the southern COB on the south flank. Therefore, we prefer to explain the
266 asymmetric seafloor spreading via ridge jumps. We postulate that ridge jumps have
267 resulted in the magnetic anomalies between M2 and the southern COB remaining on
268 the present-day north flank. This interpretation means that the five magnetic lineations
269 on the present-day north flank were generated on both flanks in the eastern part. A
270 plausible explanation is that the eastern and western parts contemporaneously initiated
271 seafloor spreading at C11n (~30 Ma) and that the spreading ridge in the eastern part
272 jumped southward twice (see section 5.2 for details).

273 In the area close to the fossil ridge, a magnetic lineation with a strong amplitude
274 (C5Dr) obliquely intersects two magnetic lineations (C5Er) on the north flank (Figure
275 3c), which indicates that a ridge jump may have occurred and been accompanied by a
276 reorientation of the spreading ridge. We identify the strong magnetic lineation as C5Dr
277 based on microfossil dating from hole U1431 (Li et al., 2015). Although complex
278 tectonism and intense post-spreading volcanism in this area have complicated the
279 magnetic anomalies (Figure 3c), we still tentatively speculate that a ridge jump
280 occurred after anomaly C5Er, associated with the synchronous reorientation of the
281 spreading ridge. This type of reorientation results from a large and rapid change in the
282 direction of plate motion, which also occurred in the Woodlark Basin and Pacific-
283 Farallon spreading center (Goodliffe et al., 1997). In the latest spreading stage, an
284 instantaneous ridge jump may have occurred after anomaly 5Cr to the east of 117.5°E

285 (Figure 3c). The ridge segment jumped southward to the location of the present-day
 286 fossil ridge, generating a larger offset near 117.5°E. These magnetic anomaly
 287 interpretations are supported by the seafloor fabric from the bathymetry of the fossil
 288 ridge region (Hsu et al., 2019; Li et al., 2002).



289
 290 **Figure 3.** Magnetic anomalies in the ESB and identifications of ridge jumps. (a) and
 291 (b) Magnetic anomalies of the conjugate areas close to the COBs on the north and south
 292 flanks, respectively. Colored lines indicate magnetic lineations between C10r and C6Cr.
 293 Red dashed lines indicate the fracture zones. White dashed lines indicate the locations
 294 of the ridge jump. M1 and M2 are a pair of conjugate negative magnetic anomalies with
 295 large amplitudes. (c) Magnetic anomalies near the fossil ridge. Double dashed lines
 296 indicate the fossil ridge. Black contour areas represent post-spreading seamounts. (d)
 297 Magnetic anomalies in the ESB. Red boxes indicate the areas of (a), (b), and (c) in the
 298 figure.

299

4.3 Euler poles

300 We calculate the finite rotation parameters by fitting the conjugate magnetic
 301 anomaly picks using the software GPlates (Müller et al., 2018) (Table 1). The fitting is
 302 performed using algorithms based on the work of Hellinger (1981) and Chang (1988).
 303 During the calculation, a grid search is first carried out for the finite rotation parameters,
 304 and the routine of the GPlates then refines the result. For each isochron, we compute
 305 15 iterations or continue until the amoeba residual is less than 10^{-10} in GPlates to obtain
 306 the finite poles. We do not calculate the finite poles of the isochrons C5Er, C6r, and
 307 C7r, because the ridge jumps destroyed the magnetic lineations and caused the paired
 308 magnetic lineations on one flank. To obtain the spreading directions and spreading rates,
 309 we calculate two sets of stage poles based on these finite poles (Table 2). One set
 310 consists of the stage poles of the north flank obtained by fixing the South China block
 311 on the north flank of the SCS and moving the blocks on the south flank. The other set
 312 consists of the stage poles of the south flank obtained by the opposite relative movement.

313 The uncertainty ellipses cannot be calculated in GPlates due to the short isochrons
 314 and the lack of large offsets in all isochrons. To test the fitting of each isochron, we
 315 rotate the magnetic anomaly picks on the south flank to the north flank based on the
 316 rotation parameters (Figure 2a). The fixed picks show good fits with rotated picks, and
 317 some small offsets on conjugate isochrons, which are important fitting constraints, also
 318 match well. Moreover, the locations of the calculated finite poles are very close to those
 319 of Briais et al. (1993) (Figure 4). Therefore, the finite poles obtained in this study are
 320 reliable.

321 **Table 1.** Finite pole parameters.

Anomalies	Age (Ma)	Longitude (°)	Latitude (°)	Angle (°)
C5Dr	17.95	107.17	3.89	3.83
C6Ar	21.54	86.97	-0.49	4.20
C6Br	23.21	83.19	0.01	4.84
C6Cr	24.42	78.13	-0.01	5.19

C8r	26.79	91.71	8.51	10.77
C9r	28.13	82.76	6.12	9.24
C10r	29.07	88.07	7.58	12.07

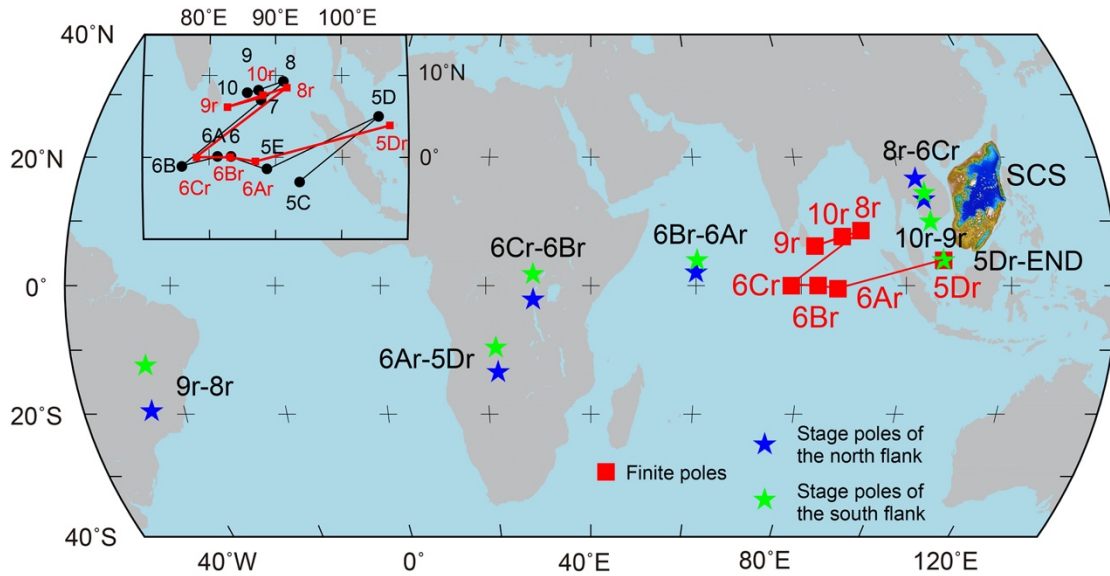
322 Positive longitudes and latitudes correspond to the eastern and northern hemispheres, respectively.

323 **Table 2.** Stage pole parameters.

Anomalies	Age span (Ma)	North flank			South flank		
		Longitude (°)	Latitude (°)	Angle (°)	Longitude (°)	Latitude (°)	Angle (°)
End–C5Dr	1.95	107.17	3.89	1.92	107.17	3.89	-1.92
C5Dr–C6Ar	3.59	22.09	-13.39	0.74	21.76	-9.58	-0.74
C6Ar–C6Br	1.67	60.00	2.03	0.35	60.23	3.93	-0.35
C6Br–C6Cr	1.21	29.00	-2.14	0.28	28.99	1.79	-0.28
C6Cr–C8r	2.37	103.27	16.63	2.98	104.57	14.38	-2.98
C8r–C9r	1.34	-46.57	-19.53	1.11	-45.91	-12.38	-1.11
C9r–C10r	0.94	104.38	13.36	1.50	105.15	9.91	-1.50

324 Positive longitudes and latitudes correspond to the eastern and northern hemispheres, respectively.

325 We plot the seven finite poles in Figure 4 from C10r (29.07 Ma) to C5Dr (17.95
326 Ma). Overall, the finite poles are located to the southwest of the SCS, conforming with
327 the V shape of the oceanic basin. The poles for C10r, C9r, and C8r are located to the
328 west of the SCS, corresponding to the westward propagation of the basin during the
329 early spreading stage. The poles for C6Cr, C6Br, and C6Ar migrated toward the
330 southwest, which indicates that the propagation changed to the southwest corresponds
331 to the opening of the SWSB. The pole for C5Dr jumped eastward to be closer to the
332 basin, reflecting the major change in the spreading direction during the late spreading
333 stage.



334

335 **Figure 4.** Locations of the finite poles and stage poles. Red squares indicate the finite
 336 poles. Blue stars indicate the stage poles of seafloor spreading in the north flank, and
 337 green stars indicate the stage poles of seafloor spreading in the south flank. In the inset,
 338 our finite poles (red squares) are compared with those (black dots) of Briais et al. (1993).

339

4.4 Spreading directions and spreading rates

340

341 We compute the spreading directions and spreading rates of the north and south
 342 flanks based on two sets of stage poles (Table 3). The average spreading directions
 343 show that the initial spreading direction of the ESB was $\sim N166^\circ$, and then the direction
 344 rotated clockwise at C9r from $\sim N166^\circ$ to $\sim N175^\circ$ (Figure 5a). After C6Cr, the
 345 spreading direction began to gradually and continuously rotate counterclockwise until
 346 C5Dr. A significant direction rotation occurring at C5Dr and the direction rotated
 347 counterclockwise from $\sim N170^\circ$ to $\sim N134^\circ$. The average spreading rates show that the
 348 initial full spreading rate of the ESB was ~ 80 mm/yr, followed by a sharp decrease to
 349 ~ 49 mm/yr at C9r (Figure 5b). From C9r to C6Br, the spreading rate varied between
 350 ~ 49 mm/yr and 64 mm/yr. Between C6Br and C5Dr, the spreading rate decreased to a
 351 relatively slow rate, between 40 mm/yr and 46 mm/yr. Since C5Dr, the spreading rate
 352 increased to ~ 58 mm/yr.

352

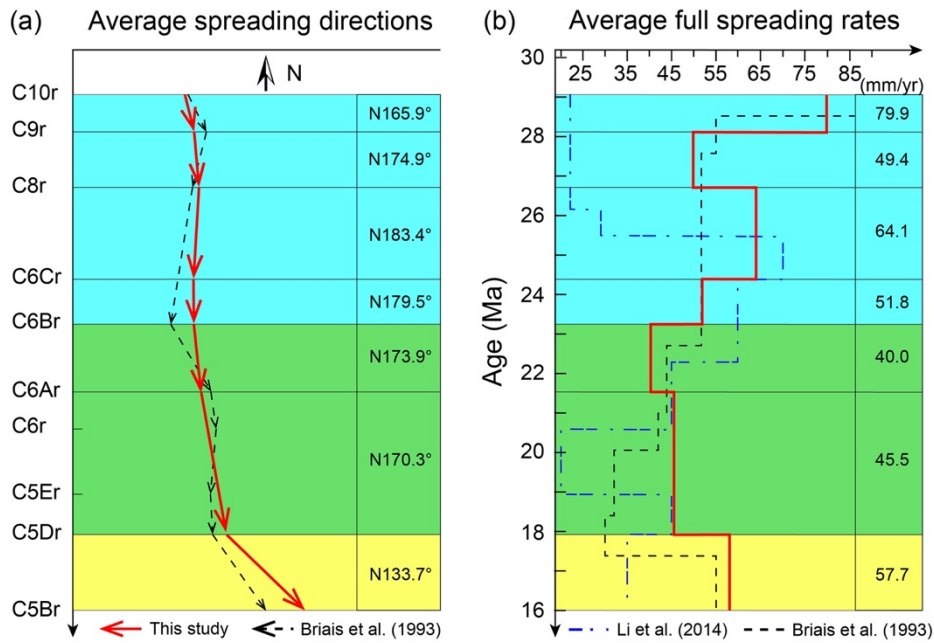
353 Based on the spreading directions and spreading rates, seafloor spreading in the
 354 ESB can be divided into three stages (Figure 5). In stage 1 (C10r–C6Br), the overall

354 spreading direction trended nearly N–S, except for the initial spreading direction
 355 (between C10r and C9r). The spreading rate was an intermediate spreading rate
 356 (average rate: ~61 mm/yr). In stage 2 (C6Br–C5Dr), the spreading directions were close
 357 to the NNW–SSE direction, corresponding to a slow spreading rate (average rate: ~44
 358 mm/yr). In stage 3 (C5Dr–cessation of seafloor spreading), the spreading direction was
 359 NW–SE. The spreading rate increased again to an intermediate spreading rate (average
 360 rate: ~58 mm/yr).

361 **Table 3.** Spreading directions and half spreading rates of the ESB

Anomalies	Age interval (Ma)	North flank		South flank	
		Spreading directions (°)	Half spreading rate (mm/yr)	Spreading directions (°)	Half spreading rate (mm/yr)
End–C5Dr	16.00–17.95	131.7	28.9	135.6	28.8
C5Dr–C6Ar	17.95–21.54	168.4	22.7	172.2	22.8
C6Ar–C6Br	21.54–23.21	171.8	20.0	176.0	20.0
C6Br–C6Cr	23.21–24.42	177.4	25.9	181.5	25.9
C6Cr–C8r	24.42–26.79	178.4	32.1	188.4	32.0
C8r–C9r	26.79–28.13	171.0	24.7	178.7	24.7
C9r–C10r	28.13–29.07	160.4	40.0	171.3	39.9

362 The directions and rates of seafloor spreading were calculated for point (red triangle in Figure 2a)
 363 on the fossil ridge based on the two sets of stage poles.



364

365 **Figure 5.** (a) Average spreading directions of the north and south flanks in the ESB.
 366 Red lines with arrows indicate the average spreading directions calculated in this study,
 367 and black dashed lines with arrows indicate the spreading directions from Briaais et al.
 368 (1993). (b) Average spreading rates of the north and south flanks in the ESB. Red lines
 369 indicate the average spreading rates calculated in this study. Black and blue dotted lines
 370 indicate the spreading rates from Briaais et al. (1993) and Li et al. (2014), respectively.
 371 Three shaded areas indicate stage 1, stage 2, and stage 3 of seafloor spreading.

372 The initial spreading rate in the ESB was up to ~80 mm/yr, potentially supporting
 373 rapid extension in the SCS margin during breakup (Ding et al., 2019; Larsen et al.,
 374 2018). The rapid extension within a relatively short period (<10 Ma) resulted in the
 375 generation of enhanced and localized magma associated with asthenospheric upwelling
 376 and decompression melting (Ding et al., 2019; Larsen et al., 2018). Nirrengarten et al.
 377 (2020) also suggested that the magmatism during initial breakup heated the pre-rift
 378 sediments to temperatures as high as 200°C. Therefore, thermal erosion related to the
 379 magma penetrating the lithosphere may have weakened the thinned lithosphere and
 380 promoted rapid rift-to-drift transition in the SCS.

381 **5 Discussion**

382 **5.1 Comparison with previous crustal age models**

383 Our crustal age model suggests that seafloor spreading in the ESB initiated at ~30
384 Ma (Figure 2), which is similar to the age proposed by Taylor and Hayes (1980,1983)
385 and Briaies et al. (1993). This age is later than the ages of 32 Ma in Barckhausen et al.
386 (2014) and ~33 Ma in Li et al. (2014). In the age model of Barckhausen et al. (2014),
387 the initial age was identified from two short magnetic profiles in the northeastern ESB.
388 Nevertheless, the spreading center may have experienced successive southward jumps
389 in this area (described in detail in the next section), which complicates the identification
390 of magnetic anomalies. The incipient age of seafloor spreading from Li et al. (2014) is
391 constrained by the breakup unconformity at Site U1435. Recently, the microfossil
392 dating and analysis of magmatism at Site U1502 from IODP Expeditions 367/368
393 suggested that the final stage of continental breakup in the ESB occurred at ~30–34 Ma
394 (Larsen et al., 2018). This result supports the initiation of seafloor spreading at ~30 Ma.

395 Li et al. (2014) proposed that seafloor spreading in the ESB initiated in the
396 northeastern part and then propagated to the west, which is contrary to our observations.
397 In this study, dozens of nearly N–S-trending magnetic profiles cover the entire northern
398 part of the ESB (Figure 1). The identifications of these profiles indicate that seafloor
399 spreading in the ESB contemporaneously initiated at C11n along the eastern and
400 western parts of the northern COB (Figures 2b and 6).

401 The youngest isochron identified in the ESB is anomaly C5Cr, under the
402 constraints of the microfossil dating of hole U1431 near the fossil ridge. Seafloor
403 spreading in the ESB ceased at ~16 Ma. This cessation age is roughly consistent with
404 the ages estimated by Briaies et al. (1993) and Li et al. (2014) but later than 20.5 Ma
405 presented by Barckhausen et al. (2014).

406 Our results partially support the age models of Taylor and Hayes (1980, 1983) and
407 Briaies et al. (1993), but propose different age interpretations for the oceanic crust in the
408 northeastern ESB and near the fossil ridge. Furthermore, the age model with a higher

409 resolution and greater coverage provides more detailed information for the dynamic
410 processes of seafloor spreading in the SCS, as discussed below.

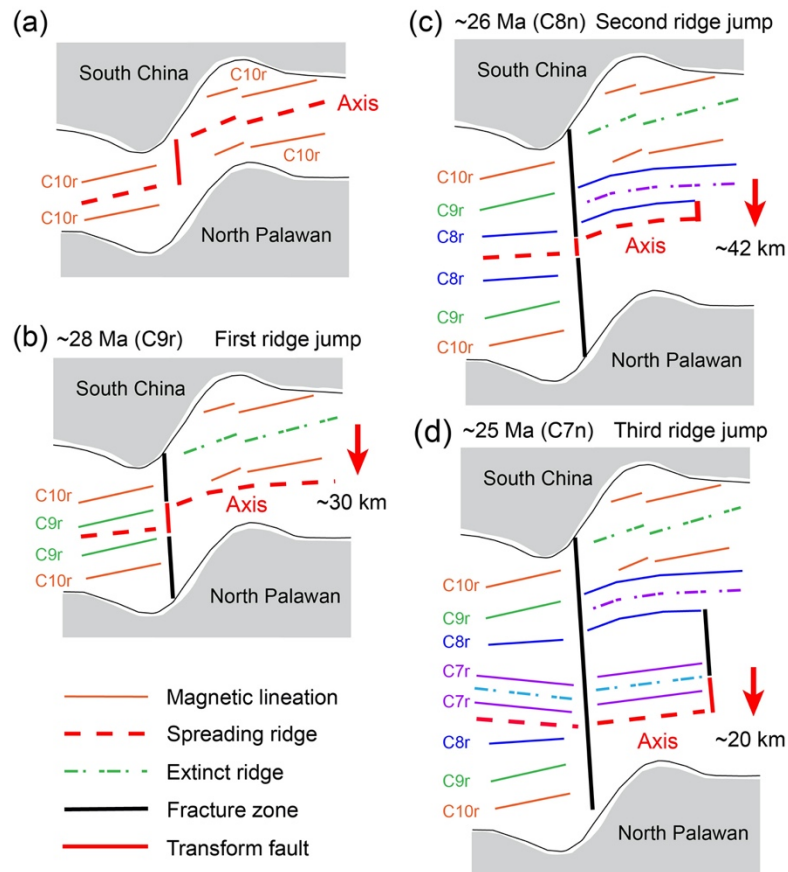
411 **5.2 Successive ridge jumps and asymmetry of the oceanic crust**

412 The geometry of the ESB exhibits an asymmetry with a smaller area on the south
413 flank of the fossil ridge (Figure 2). Especially in the eastern part, the north flank has
414 accreted ~450 km of oceanic crust from the fossil ridge to the northern COB, which is
415 1.5 times that of the south flank. Moreover, the magnetic anomalies on both flanks also
416 show distinct asymmetry in amplitudes and numbers from C6Cr to COB (Figure 3).
417 The geometric and magnetic asymmetry is thought to be the result of ridge jumps
418 (Briais et al., 1993; Ding et al., 2018).

419 We present a successive ridge jump pattern to explain the distinct geometric and
420 magnetic asymmetry (Figures 3 and 6). In this pattern, three ridge jumps occurred
421 during the early spreading stage. The first ridge jump occurred in the eastern part at ~28
422 Ma (C9r) and jumped southward by ~30 km, which left the paired magnetic lineations
423 C10r on the present-day north flank (Figure 6b). This ridge jump was a synchronous
424 reorientation involving minor clockwise rotation (Figures 5a and 6b). Ding et al. (2018)
425 identified two conjugate lower crustal reflector groups from a multichannel seismic
426 transect in the eastern part, which may support this ridge jump. The second ridge jump
427 occurred in the eastern part at ~26 Ma (C8n) and jumped southward by ~42 km. The
428 paired magnetic lineations C8r were left on the present-day north flank (Figure 6c). The
429 third ridge jump occurred through the entire ESB at ~25 Ma and jumped southward by
430 ~20 km, leaving the paired magnetic lineations C7r on the present-day north flank
431 (Figure 6d). This ridge jump has also been identified by previous studies (Barckhausen
432 et al., 2014; Briais et al., 1993; Li et al., 2014; Taylor & Hayes, 1983). Although these
433 ridge jumps are only observed in the northern ESB, they may also have occurred
434 simultaneously in a large area in the east of the SCS that has subducted beneath the
435 Philippine sea plate.

436 The three southward ridge jumps caused a total distance difference of
437 approximately 184 km between the two flanks from C6Cr to COBs in the eastern part
438 and left magnetic lineations C10r–C7r on the present-day north flank. Meanwhile,
439 successive ridge jumps eliminated a ~70 km-long offset between the eastern and
440 western parts and aligned magnetic lineation C6r across the entire ESB (Figure 6).

441 Successive ridge jumps are usually ascribed to the effects of hot spots or plumes
442 on ridges (Brozena et al., 1990; Mittelstaedt et al., 2011; Müller et al., 1998). More
443 ridge jumps could occur in young plates with slow spreading rates (Mittelstaedt et al.,
444 2011). However, there is no clear evidence of plumes beneath the SCS and the
445 spreading rates during the jumping are also intermediate spreading rates (~49-64 mm/yr)
446 (Figure 5b). In other regions away from hot spots or plumes, ridge jumps during the
447 initiation of seafloor spreading have also been observed (Benes et al., 1997;
448 d'Acremont et al., 2010; Taylor et al., 1999, 2009). Analyzing the evolution of the
449 spreading segments in these regions, Taylor et al. (2009) suggested that ridge jumps are
450 common processes that reorganize ridge orientation. When the ridge jumps at C9r and
451 C8n occurred in the SCS, the corresponding spreading direction rotated by 9° and 8.5°,
452 respectively (Figure 5a). Although the spreading direction at C7n has not been
453 calculated, the strike of the spreading ridge rotated from the NWW–SEE-trending at
454 C7r to the nearly E-W-trending at C6Cr (Figures 2 and 3), indicating that the spreading
455 direction also changed slightly when ridge jump occurred at C7n. Therefore, the
456 successive ridge jumps may result from the frequent reorientation of seafloor spreading
457 in the SCS, which reflects the instability of the dynamic processes of the basin during
458 the early spreading stage.



459

460 **Figure 6.** Schematic diagram of successive ridge jumps during the early spreading
 461 stage.

462 **5.3 Rotations of the spreading direction and fracture zones**

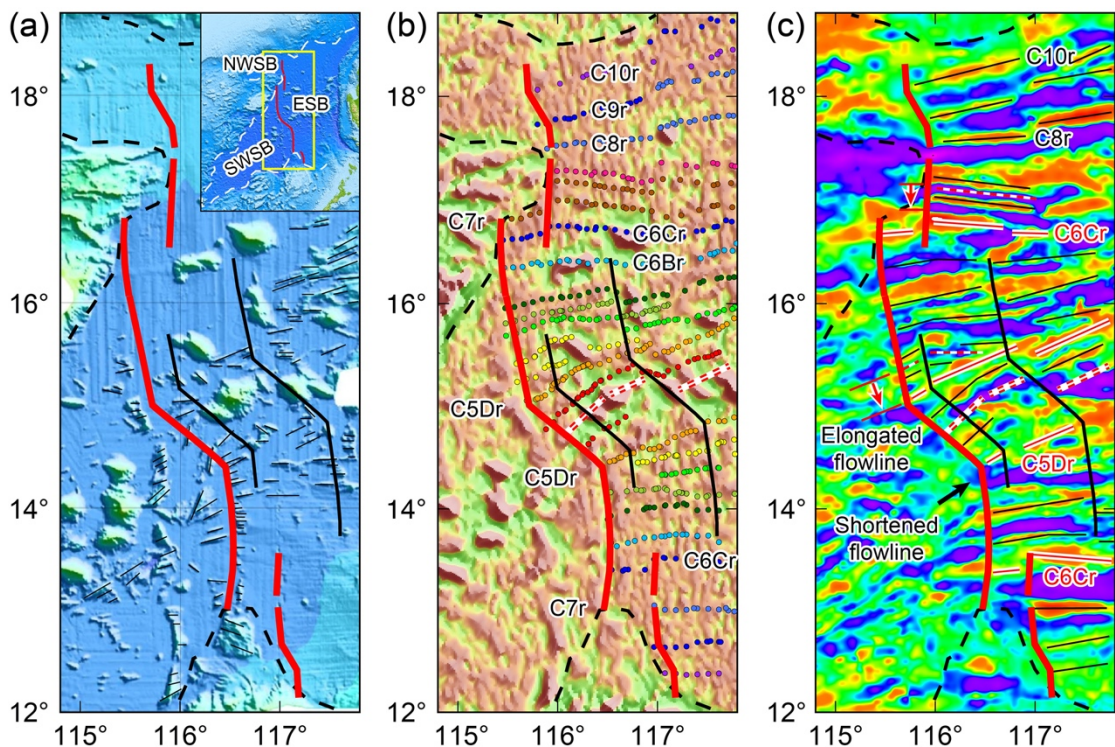
463 The continuous counterclockwise rotations of seafloor spreading in the SCS
 464 reorganized the orientation and segmentation of the spreading ridge. From C6Cr to
 465 C5Dr, the counterclockwise rotations caused a $\sim 13^\circ$ change in the spreading direction.
 466 The slow and/or relatively small rotation resulted in a gradual rotation and segmentation
 467 of the spreading ridge. The spreading ridge gradually rotated from nearly E–W at C6Cr
 468 to NEE–SWW at C5Er and was broken into several segments connected by small
 469 transform faults (Figures 2 and 7). The gradual ridge rotation is a typical reorientation
 470 type, which occurred repeatedly in the north-eastern Pacific and Shikoku–Parece Vela
 471 Basins (Kasuga & Ohara, 1997; Menard & Atwater, 1968; Okino et al., 1999). At C5Dr,
 472 a significant counterclockwise rotation caused a $\sim 37^\circ$ change in the spreading direction.
 473 The larger and more rapid rotation resulted in the spreading ridge reorientation by a

474 synchronous jump. The reoriented spreading ridges (C5Dr) obliquely intersect the
475 existing seafloor and the abandoned spreading center. Similar processes also occurred
476 in the recent spreading stage of the Woodlark Basin (Goodliffe et al., 1997).

477 The transform faults between the spreading ridge segments formed a series of
478 fracture zones with seafloor spreading. These fracture zones record the changes in the
479 spreading direction and seafloor spreading history of the SCS. However, the locations
480 and trends of the fracture zones are still unclear because they are covered by 1-2 km of
481 sediment (Ruan et al., 2016). The negative VGG anomaly could provide information
482 for the sediment-covered fracture zones (Hwang & Chang, 2014; Sandwell et al., 2014)
483 and can be compared with the fracture zones depicted by the flowlines (Pitman &
484 Talwan, 1972). Therefore, we calculate synthetic flowlines based on the stage poles
485 and attempt to determine the fracture zones by comparing it with the VGG, outcropping
486 geomorphic features, and magnetic anomalies.

487 The Zhongnan fracture zone, the boundary of the ESB with the SWSB and NWSB,
488 is the most important fracture zone in the SCS, and its formation throughout the entire
489 opening period of the SCS. The negative VGG anomaly shows that the Zhongnan
490 fracture zone between the ESB and the NWSB is nearly N–S-trending along
491 approximately 115.7°E before C10r, NNW–SSE-trending between C10r and C9r, and
492 then extends southward along the COB on the northeast of Zhongsha Islands after C9r
493 (Figure 7b). The changes of the fracture zone trend are consistent with the evolution of
494 the spreading direction (Figure 5a). The offset in the lineation C6Cr near 115.9°E and
495 continuous lineation C6Br indicate the fracture zone extending southward terminated
496 before C6Br. Further west, a young fracture zone began to form at C7r, with the
497 westward propagation of seafloor spreading. From C7r to C5Dr, the fracture zone
498 extended southward along approximately 115.5°E and is slightly concave to the east.
499 The concave corresponds to gradual counterclockwise rotation in the spreading
500 direction between C6Cr and C5Dr. After C5Dr, the trend of the fracture zone rotated
501 suddenly to NW–SE-trending shown by the negative VGG anomaly, geomorphic

502 features, and magnetic anomalies. The prominent rotation is associated with the major
 503 counterclockwise rotation in the spreading direction at C5Dr (Figure 5a). At the same
 504 time, a synchronous ridge jump occurred with counterclockwise rotation. The jump
 505 caused the Zhongnan fracture zone in the north flank to be elongated by ~40 km and
 506 that in the south flank to be shorten by the same distance. The flowlines are adjusted
 507 based on the jump and indicate that the Zhongnan fracture zone in the south flank
 508 locates on the west of the outcropping ridge and extends along the ridge southward to
 509 COB (Figure 7a). The location of the fracture zone is also supported by the magnetic
 510 lineations C6Cr with conjugated small offsets (Figure 7c). Therefore, the Zhongnan
 511 fracture zone may be a discontinuous fracture zone, which is composed of the fracture
 512 zone before C6Br and the subsequent S-shaped fracture zone. To the east, we also
 513 identify two additional fracture zones resulted from the reorientation and segmentation
 514 of the spreading ridge (Figure 7).



515

516 **Figure 7.** (a) Bathymetric map located in the central part of the South China Sea (SCS).
 517 Short black lines indicate outcropping seafloor spreading lineaments. (b) Vertical
 518 gravity gradient map (Sandwell et al., 2014) with the magnetic picks. (c) Magnetic

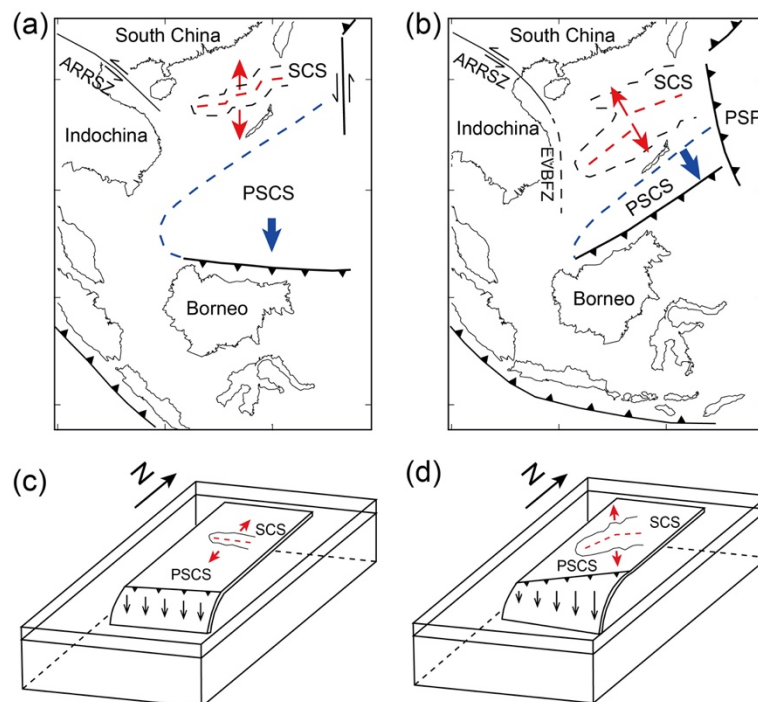
519 anomalies map with the magnetic lineations. Thick red lines indicate the Zhongnan
520 fracture zone. Thin black lines indicate two fracture zones parallel to the Zhongnan
521 fracture zone. Red dashed lines indicate the locations of the ridge jump.

522 **5.4 Dynamic processes of the evolution of the SCS**

523 Spreading ridge jumps and rotations are common processes that reorganize the
524 orientation of ridges in marginal basins, such as the Woodlark Basin (Goodliffe et al.,
525 1997; Taylor et al., 2009), the Shikoku–Parece Vela Basin (Kasuga & Ohara, 1997;
526 Okino et al., 1999). The occurrence of these processes is a response to changes in plate
527 motion around the basins (Goodliffe et al., 1997). Similarly, seafloor spreading of the
528 SCS, located at the junction of three major plates, may have also been potentially
529 associated by the surrounding plates and microplates tectonics. The ages of many
530 spreading processes in the SCS were coeval with the tectonic events of the surrounding
531 plates. For example, an instantaneous ridge jump occurred at 25 Ma, which coincided
532 with the period of the most important Cenozoic plate boundary reorganization. In this
533 period, the southward extrusion of Indochina block along the EVBFZ ceased (Fyhn et
534 al., 2009a, 2009b), the Ontong Java Plateau collided with the Melanesian Arc, and the
535 northern Australian margin collided with the southern Philippine plate (Hall, 2002; Hall
536 et al., 1995). The termination of seafloor spreading in the SCS at ~16 Ma was coeval
537 with the collision of the Dangerous Grounds–Reed Bank microcontinents and northern
538 Borneo (Holloway, 1982; Hutchison et al., 2000). The significant counterclockwise
539 rotations of seafloor spreading in the SCS at ~18 Ma also coincided with the termination
540 of Indochina block left-lateral movements along the ARRSZ (Leloup et al., 1993).
541 However, Indochina block was extruded southward along the EVBFZ on the west of
542 the SCS, and the extrusion along the EVBFZ terminated at ~25 Ma (Fyhn et al., 2009a,
543 2009b). Hall (2002) suggested that subduction-related controls are far more important
544 than other processes in most parts of Southeast Asian and West Pacific. Moreover, the
545 spreading pattern in the Shikoku–Parece Vela Basin caused by the oblique subduction
546 of the Pacific plate is very similar to that in the SCS. Therefore, we tentatively discuss

547 the possible causes for the counterclockwise rotations of seafloor spreading in the SCS
548 based on the main framework of the slab pull models and surrounding plate tectonics.

549 In this model, the PSCS slab subducted southward beneath the Borneo, while
550 Borneo rotated counterclockwise by $\sim 50^\circ$ between 25 Ma and 10 Ma (Fuller et al.,
551 1999). As the rotation of Borneo, the amount of subducted slab increased from the west
552 to the east along the subduction zone (Sibuet et al., 2016). A greater slab pull may have
553 arisen in the eastern subduction zone because the net slab pull force increases with the
554 amount of subducted slab (Schellart, 2004) (Figure 8), which could cause the south
555 flank of the SCS to drift southeastward. By 20 Ma to 15 Ma, the initial subduction of
556 the eastern SCS beneath the western Philippine plate may have further provided space
557 for the eastward component of the south flank drift and triggered the prominent
558 counterclockwise rotation of the spreading direction of the SCS at 18 Ma (C5Dr)
559 (Figure 8). Therefore, the combined effect of the changes in the direction of the PSCS
560 slab pull and the SCS slab subduction beneath the Philippine plate could be a possible
561 explanation for the counterclockwise rotation of seafloor spreading in the SCS.



562

563 **Figure 8.** Structural sketch of the study area. (a) The PSCS subducted southward during
564 the early spreading stage of the SCS. (b) The subduction direction of the PSCS
565 gradually changed to the southeast, with the counterclockwise rotation of Borneo. (c)
566 and (d) are schematic models of (a) and (b), respectively. ARRSZ, Ailaoshan-Red River
567 Shear Zone. EVBFZ, East Vietnam Boundary Fault Zone. PSP, Philippine Sea Plate.

568 **6 Conclusions**

569 We reinterpreted the magnetic anomalies in the ESB based on the new marine
570 magnetic dataset and present a high-resolution crustal age model. Age model shows
571 that seafloor spreading initiated contemporaneously along the eastern and western parts
572 of the COB at ~30 Ma (C11n) and ceased at ~16 Ma (C5Br). The average full spreading
573 rate of the ESB is 53 mm/yr, which is an intermediate spreading rate.

574 During the early spreading stage, three ridge jumps occurred at C9r, C8n, and C7n,
575 resulting in the distinct geometric and magnetic asymmetry of the ESB. A synchronous
576 ridge jump with counterclockwise rotation occurred at C5Dr, obliquely intersecting the
577 existing seafloor and the abandoned spreading center. After C6Cr, the seafloor
578 spreading continuously rotated counterclockwise, reorganizing the segmentation of the
579 spreading ridge and forming a series of S-shaped fracture zones.

580 Successive spreading ridge jumps and continuous rotations of seafloor spreading
581 are important features in the opening processes of the SCS, which may have been
582 associated with the surrounding plate tectonics. We speculate that the counterclockwise
583 rotations of seafloor spreading may be related to the changes in the direction of the
584 PSCS slab pull and the eastward subduction of the SCS.

585 **Acknowledgments**

586 We appreciate the helpful discussions with Fan Zhang, Zhiyuan Zhou, Chunguo Yang,
587 Zhaocai Wu, and Zhongyan Shen. This research was supported by the National Nature
588 Science Foundation of China (grant 41890811, grant 41976079, grant 41576065, and
589 grant 40776036), the National Program on Global Change and Air-Sea Interaction
590 (GASI-GEOGE-05), and the National Major Scientific Instruments and Equipment
591 Development Project of China (2014YQ100817-06). We used the Modmag software
592 (Mendel et al., 2005) and GPlates software (Müller et al., 2018) in this work. Most of
593 the figures were made using the GMT software (Wessel et al., 2019). The magnetic
594 picks are available from <https://github.com/QingshengGuan/SCS-Magnetic-picks.git>.

595 **References**

- 596 Barckhausen, U., Engels, M., Franke, D., Ladage, S., & Pubellier, M. (2014). Evolution
597 of the South China Sea: Revised ages for breakup and seafloor spreading. *Marine and*
598 *Petroleum Geology*, 58, 599-611. doi:10.1016/j.marpetgeo.2014.02.022
- 599 Barckhausen, U., & Roeser, H. A. (2004). Seafloor spreading anomalies in the South
600 China Sea revisited. In P. Clift, W. R. Kuhnt, P. Wang, & D. Hayes (Eds.), *Continent-*
601 *ocean interactions within East Asian marginal seas*, *Geophysical Monograph Series*
602 (Vol. 149). Washington, DC: American Geophysical Union.
- 603 Benes, V., Bocharova, N., Popov, E., Scott, S., & Zonenshain, L. (1997). Geophysical
604 and morpho-tectonic study of the transition between seafloor spreading and continental
605 rifting, western Woodlark Basin, Papua New Guinea. *Marine Geology*, 142(1), 85-98.
606 doi:10.1016/S0025-3227(97)00042-X
- 607 Briais, A., Patriat, P., & Tapponnier, P. (1993). Updated interpretation of magnetic
608 anomalies and seafloor spreading stages in the South China Sea: implications for the
609 Tertiary tectonic of Southeast Asia. *Journal of Geophysical Research*, 98(B4), 6299-
610 6328. doi:10.1029/92JB02280
- 611 Brozena, J. M., & White, R. S. (1990). Ridge jumps and propagations in the South
612 Atlantic Ocean. *Nature*, 348(6297), 149-152. doi: 10.1038/348149a0
- 613 Chang, T. (1988). Estimating the Relative Rotation of Two Tectonic Plates from
614 Boundary Crossings. *Journal of the American Statistical Association*, 83(404), 1178-
615 1183. doi:10.1080/01621459.1988.10478717
- 616 d'Acremont, E., Leroy, S., Maia, M., Gente, P., & Autin, J. (2010). Volcanism, jump
617 and propagation on the Sheba ridge, eastern Gulf of Aden: segmentation evolution and
618 implications for oceanic accretion processes. *Geophysical Journal International*,
619 180(2), 535-551. doi:10.1111/j.1365-246X.2009.04448.x

620 Ding, W., Sun, Z., Dadd, K., Fang, Y., & Li, J. (2018). Structures within the oceanic
621 crust of the central South China Sea basin and their implications for oceanic
622 accretionary processes. *Earth and Planetary Science Letters*, 488, 115-125.
623 doi:10.1016/j.epsl.2018.02.011

624 Ding, W., Sun, Z., Mohn, G., Nirrengarten, M., Tugend, J., Manatschal, G., & Li, J.
625 (2019). Lateral evolution of the rift-to-drift transition in the South China Sea: Evidence
626 from multi-channel seismic data and IODP Expeditions 367&368 drilling results. *Earth
627 and Planetary Science Letters*, 531. doi:10.1016/j.epsl.2019.115932

628 Fan, C., Xia, S., Zhao, F., Sun, J., Cao, J., Xu, H., & Wan, K. (2017). New insights into
629 the magmatism in the northern margin of the South China Sea: Spatial features and
630 volume of intraplate seamounts. *Geochemistry, Geophysics, Geosystems*, 18(6), 2216-
631 2239. doi:10.1002/2016gc006792

632 Fuller, M., Ali, J. R., Moss, S. J., Frost, G. M., Richter, B., & Mahfi, A. (1999).
633 Paleomagnetism of Borneo. *Journal of African Earth Sciences*, 17(1-2), 3-24.
634 doi:10.1016/S0743-9547(98)00057-9

635 Fyhn, M. B. W., Boldreel, L. O., & Nielsen, L. H. (2009a). Geological development of
636 the Central and South Vietnamese margin: Implications for the establishment of the
637 South China Sea, Indochinese escape tectonics and Cenozoic volcanism.
638 *Tectonophysics*, 478(3-4), 184-214. doi:10.1016/j.tecto.2009.08.002

639 Fyhn, M. B. W., Nielsen, L. H., Boldreel, L. O., Thang, L. D., Bojesen-Koefoed, J.,
640 Petersen, H. I., . . . Abatzis, I. (2009b). Geological evolution, regional perspectives and
641 hydrocarbon potential of the northwest Phu Khanh Basin, offshore Central Vietnam.
642 *Marine and Petroleum Geology*, 26(1), 1-24. doi:10.1016/j.marpetgeo.2007.07.014

643 Gao, J. Y., & Liu, B. H. (2014). *China's offshore ocean-marine geophysics*. Beijing:
644 China Ocean Press.

645 Gee, J. S., & Kent, D. V. (2007). Source of oceanic magnetic anomalies and the
646 geomagnetic polarity timescale. In G. Schubert (Ed.), *Treatise on geophysics* (Vol. 5,
647 pp. 455-507). Amsterdam: Elsevier.

648 Gilley, L. D., Harrison, T. M., Leloup, P. H., Ryerson, F. J., Lovera, O. M., & Wang,
649 J.-H. (2003). Direct dating of left-lateral deformation along the Red River shear zone,
650 China and Vietnam. *Journal of Geophysical Research: Solid Earth*, 108(B2).
651 doi:10.1029/2001jb001726

652 Goodliffe, A. M., Taylor, B., Martinez, F., Hey, R., Maeda, K., & Ohno, K. (1997).
653 Synchronous orientation of the Woodlark Basin Spreading Center. *Earth and*
654 *Planetary Science Letters*, 146, 233-242. doi:10.1016/S0012-821X(96)00227-0

655 Hall, R. (2002). Cenozoic geological and plate tectonic evolution of SE Asia and the
656 SW Pacific: computer-based reconstructions, model and animations. *Journal of African*
657 *Earth Sciences*, 20(4), 353-431. doi:10.1016/S1367-9120(01)00069-4

658 Hall, R., Ali, J. R., Anderson, C. D., & Baker, S. J. (1995). Origin and motion history
659 of the Philippine Sea Plate. *Tectonophysics*, 251(1-4), 229-250. doi:10.1016/0040-
660 1951(95)00038-0

661 Hellinger, S. J. (1981). The uncertainties of finite rotations in plate tectonics. *Journal*
662 *of Geophysical Research: Solid Earth*, 86(B10), 9312-9318.
663 doi:10.1029/JB086iB10p09312

664 Holloway, N. H. (1982). North Palawan Block, Philippines—Its relation to Asian
665 mainland and role in evolution of South China Sea. *The American Association of*
666 *Petroleum Geologists Bulletin*, 66(9), 1355-1383.

667 Hsu, S.-K., Armada, L. T., Yeh, Y.-C., Dimalanta, C. B., Tsai, C.-H., & Bacolcol, T.
668 (2019). The seafloor fabrics and evolution of a propagated rift system in the South
669 China Sea: 2019 AGU Fall Meeting, T43F-0508.

670 Hutchison, C. S., Bergman, S. C., Swauger, D. A., & Graves, J. E. (2000). A Miocene
671 collisional belt in north Borneo: uplift mechanism and isostatic adjustment quantified
672 by thermochronology. *Journal of the Geological Society*, 157(4), 783-793.
673 doi:10.1144/jgs.157.4.783

674 Hwang, C., & Chang, E. T. (2014). Geophysics. Seafloor secrets revealed. *Science*,
675 346(6205), 32-33. doi:10.1126/science.1260459

676 Kasuga, S., & Ohara, Y. (1997). A new model of back-arc spreading in the Parece Vela
677 Basin, northwest Pacific margin. *The Island Arc*, 6(3), 316-326. doi:10.1111/j.1440-
678 1738.1997.tb00181.x

679 Koppers, A. P. (2014). On the $^{40}\text{Ar}/^{39}\text{Ar}$ dating of low-potassium ocean crust basalt
680 from IODP Expedition 349, South China Sea: 2014 AGU Fall Meeting, T31E-03.

681 Larsen, H. C., Mohn, G., Nirrengarten, M., Sun, Z., Stock, J., Jian, Z., . . . Zhong, L.
682 (2018). Rapid transition from continental breakup to igneous oceanic crust in the South
683 China Sea. *Nature Geoscience*, 11(10), 782-789. doi:10.1038/s41561-018-0198-1

684 Leloup, P. H., Arnaud, N., Lacassin, R., Kienast, J. R., Harrison, T. M., Trong, T. T.
685 P., . . . Tapponnier, P. (2001). New constraints on the structure, thermochronology, and
686 timing of the Ailao Shan-Red River shear zone, SE Asia. *Journal of Geophysical*
687 *Research: Solid Earth*, 106(B4), 6683-6732. doi:10.1029/2000jb900322

688 Leloup, P. H., Harrison, T. M., Ryerson, F. J., Wenji, C., Qi, L., Tapponnier, P., &
689 Lacassin, R. (1993). Structural, petrological and thermal evolution of a Tertiary ductile
690 strike-slip shear zone, Diancang Shan, Yunnan. *Journal of Geophysical Research:*
691 *Solid Earth*, 98(B4), 6715-6743. doi:10.1029/92jb02791

692 Li, C. F., Lin, J., Kulhanek, D. K. & Expedition 349 Scientists. (2015). Expedition 349
693 summary. In Proc. IODP (eds Li, C.-F., Lin, J., Kulhanek, D. K. & Expedition 349
694 Scientists) Vol. 349. doi:10.14379/iodp.proc.349.101.2015

695 Li, C. F., Xu, X., Lin, J., Sun, Z., Zhu, J., Yao, Y. J., . . . Zhang, G. L. (2014). Ages and
696 magnetic structures of the South China Sea constrained by deep tow magnetic surveys
697 and IODP Expedition 349. *Geochemistry Geophysics Geosystems*, *15*, 4958-4983.
698 doi:10.1002/2014GC005567

699 Li, J. B., Ding, W. W., Wu, Z. Y., Zhang, J., & Dong, C. Z. (2012). The propagation of
700 seafloor spreading in the southwestern subbasin, South China Sea. *Chinese Science*
701 *Bulletin*, *57*(24), 3182-3191. doi:10.1007/s11434-012-5329-2

702 Li, J. B., Jin, X. L., & Gao, J. Y. (2002). Tectonic and geomorphological study of the
703 South China Sea in the late spreading stage. *Science in China (Series D)*, *32*(3), 239-
704 248. doi:10.3969/j.issn.1674-7240.2002.03.009

705 Menard, H. W., & Atwater, T. (1968). Changes in direction of sea floor spreading.
706 *Nature*, *219*(5153), 463-467. doi: 10.1038/219463a0

707 Mendel, V., Munschy, M., & Sauter, D. (2005). MODMAG, a MATLAB program to
708 model marine magnetic anomalies. *Computers & Geosciences*, *31*(5), 589-597.
709 doi:10.1016/j.cageo.2004.11.007

710 Mittelstaedt, E., Ito, G., & van Hunen, J. (2011). Repeat ridge jumps associated with
711 plume-ridge interaction, melt transport, and ridge migration. *Journal of Geophysical*
712 *Research*, *116*(B1). doi:10.1029/2010jb007504

713 Müller, R. D., Cannon, J., Qin, X., Watson, R. J., Gurnis, M., Williams, S., . . .
714 Zahirovic, S. (2018). GPlates: Building a Virtual Earth Through Deep Time.
715 *Geochemistry, Geophysics, Geosystems*, *19*(7), 2243-2261.
716 doi:10.1029/2018gc007584

717 Müller, R. D., Roest, W. R., & Royer, J.-Y. (1998). Asymmetric seafloor spreading
718 caused by ridge-plume interactions. *Nature*, *396*(6710), 455-459. doi:10.1038/24850

719 Nirrengarten, M., Mohn, G., Schito, A., Corrado, S., Gutiérrez-García, L., Bowden, S.
720 A., & Despinois, F. (2020). The thermal imprint of continental breakup during the

721 formation of the South China Sea. *Earth and Planetary Science Letters*, 531.
722 doi:10.1016/j.epsl.2019.115972

723 Okino, K., Ohara, Y., Kasuga, S., & Kato, Y. (1999). The Philippine Sea: New survey
724 results reveal the structure and the history of the marginal basins. *Geophysical Research*
725 *Letters*, 26(15), 2287-2290. doi:10.1029/1999gl900537

726 Pitman, W. C., & Talwan, M. (1972). Sea-Floor Spreading in the North Atlantic.
727 *Geological Society of America Bulletin*, 83(3), 619-646. doi:10.1130/0016-
728 7606(1972)83[619:SSITNA]2.0.CO;2

729 Ruan, A. G., Wei, X. D., Niu, X. W., Zhang, J., Dong, C. Z., Wu, Z. L., & Wang, X. Y.
730 (2016). Crustal structure and fracture zone in the Central Basin of the South China Sea
731 from wide angle seismic experiments using OBS. *Tectonophysics*.
732 doi:10.1016/j.tecto.2016.09.022

733 Sandwell, D. T., Müller, R. D., Smith, W. H. F., Garcia, E., & Francis, R. (2014). New
734 global marine gravity model from CryoSat-2 and Jason-1 reveals buried tectonic
735 structure. *Science*, 346(6205), 65-67. doi:10.1126/science.1258213

736 Schärer, U., Tapponnier, P., Lacassin, R., Leloup, P. H., Zhong, D., & Ji, S. C. (1990).
737 Intraplate tectonics in Asia: a precise age for large-scale Miocene movement along the
738 Ailao Shan-Red River shear zone, China. *Earth and Planetary Science Letters*, 97(1),
739 65-77. doi:10.1016/0012-821X(90)90099-J

740 Schellart, W. P. (2004). Quantifying the net slab pull force as a driving mechanism for
741 plate tectonics. *Geophysical Research Letters*, 31(7). doi:10.1029/2004gl019528

742 Sibuet, J. C., Yeh, Y. C., & Lee, C. S. (2016). Geodynamics of the South China Sea.
743 *Tectonophysics*, 692, 98-119. doi:10.1016/j.tecto.2016.02.022

744 Sun, Z., Jian, Z., Stock, J. M., Larsen, H. C., Klaus, A., Alvarez Zarikian, C. A., & the
745 Expedition 367/368 Scientists. (2018). Proceedings of the International Ocean
746 Discovery Program Volume 367/368. doi:10.14379/iodp.proc.367368.101.2018

747 Tapponnier, P., Lacassin, R., Leloup, P. H., Schärer, U., Dalai, Z., Haiwei, W., . . .
748 Jiayou, Z. (1990). The Ailao Shan/Red River metamorphic belt: Tertiary left-lateral
749 shear between Indochina and South China. *Nature*, *343*(6257), 431-437.
750 doi:10.1038/343431a0

751 Tapponnier, P., Peltzer, G., Le Dain, A. Y., Armijo, R., & Cobbold, P. (1982).
752 Propagating extrusion tectonics in Asia: New insights from simple experiments with
753 plasticine. *Geology*, *10*(12). doi:10.1130/0091-7613(1982)10<611:Petian>2.0.Co;2

754 Taylor, B., Goodliffe, A., & Martinez, F. (1999). How continents break up: Insights
755 from Papua New Guinea. *Journal of Geophysical Research: Solid Earth*, *104*(B4),
756 7497-7512. doi:10.1029/1998jb900115

757 Taylor, B., Goodliffe, A., & Martinez, F. (2009). Initiation of transform faults at rifted
758 continental margins. *Comptes Rendus Geoscience*, *341*(5), 428-438.
759 doi:10.1016/j.crte.2008.08.010

760 Taylor, B., & Hayes, D. E. (1980). The tectonic evolution of the South China Basin. In
761 D. E. Hayes (Ed.), *The Tectonic and Geologic Evolution of Southeast Asian Seas and*
762 *Islands: Part 1* (Vol. 23, pp. 89-104). Washington, DC: American Geophysical Union.

763 Taylor, B., & Hayes, D. E. (1983). Origin and History of the South China Sea Basin.
764 In D. E. Hayes (Ed.), *The Tectonic and Geologic Evolution of Southeast Asian Seas*
765 *and Islands: Part 2, Geophysical Monograph Series* (Vol. 27, pp. 23-56). Washington,
766 DC: American Geophysical Union.

767 Thébault, E., Finlay, C. C., Beggan, C. D., Alken, P., Aubert, J., Barrois, O., . . . Zvereva,
768 T. (2015). International Geomagnetic Reference Field: the 12th generation. *Earth,*
769 *Planets and Space*, *67*(1), 79. doi:10.1186/s40623-015-0228-9

770 Tozer, B., Sandwell, D. T., Smith, W. H. F., Olson, C., Beale, J. R., & Wessel, P. (2019).
771 Global Bathymetry and Topography at 15 Arc Sec: SRTM15+. *Earth and Space*
772 *Science*, *6*(10), 1847-1864. doi:10.1029/2019ea000658

773 Wessel, P., Luis, J. F., Uieda, L., Scharroo, R., Wobbe, F., Smith, W. H. F., & Tian, D.
774 (2019). The Generic Mapping Tools Version 6. *Geochemistry, Geophysics, Geosystems*,
775 20(11), 5556-5564. doi:10.1029/2019gc008515

776 Wu, J., Suppe, J., Lu, R., & Kanda, R. (2016). Philippine Sea and East Asian plate
777 tectonics since 52 Ma constrained by new subducted slab reconstruction methods.
778 *Journal of Geophysical Research: Solid Earth*, 121(6), 4670-4741.
779 doi:10.1002/2016jb012923

780 Yao, B. C. (1995). Characteristics and tectonic significance of Zhongnan-Liyue fault.
781 *Geological Research of South China Sea (in Chinese)*, 7.

782 Zahirovic, S., Seton, M., & Müller, R. D. (2014). The Cretaceous and Cenozoic tectonic
783 evolution of Southeast Asia. *Solid Earth*, 5(1), 227-273. doi:10.5194/se-5-227-2014

784 Zhang, T., Dyment, J., & Gao, J. Y. (2019). Age of the Canada basin, Arctic Ocean:
785 indications from high-resolution magnetic data. *Geophysical Research Letters*, 46(23),
786 13712-13721. doi:10.1029/2019gl085736

787 Zhang, T., Gao, J. Y., Li, J. B., WU, Z. C., Wu, Z. L., Zhao, L. H., . . . Zhou, Z. Y.
788 (2012). The magnetic lineation identifications and segmentation of the northwestern
789 sub-basin in the South China Sea. *Chinese Journal of Geophysics-Chinese Edition*,
790 55(9), 3163-3172. doi:10.6038/j.isn.0001-5733.2012.09.034